IEEE Access
Multidisciplinary ⋮ Rapid Review ⋮ Open Access Journal

Received 20 October 2025, accepted 12 November 2025, date of publication 24 November 2025,
date of current version 4 December 2025.

Digital Object Identifier 10.1109/ACCESS.2025.3636385

RESEARCH ARTICLE

Intuitionistic Fuzzy Cognitive Map for Disease Transmission Risk Assessment in Ventilated Indoor Spaces

MICHAEL D. VASILAKAKIS, GEORGIOS TRIANTAFYLLOU, AND DIMITRIS K. IAKOVIDIS, (Senior Member, IEEE)
Department of Computer Science and Biomedical Informatics, University of Thessaly, 351 31 Lamia, Greece

Corresponding author: Dimitris K. Iakovidis (diakovidis@uth.gr)

This paper is supported by the European Union's Horizon Europe Research and Innovation Actions programme under grant agreement No 101069937, project name: HS4U (HEALTHY SHIP 4U). Views and opinions expressed are those of the author(s) only and do not necessarily reflect those of the European Union or the European Climate, Infrastructure, and Environment Executive Agency. Neither the European Union nor the granting authority can be held responsible for them.

ABSTRACT Cruise ships remain a popular vacation choice for millions of travelers annually. However, the on-board environment, characterized by high population density and close-contact settings in ventilated indoor spaces, creates ideal conditions for the spread of highly airborne transmissible respiratory diseases, such as SARS-COV-2. This study focuses on an effective framework for managing airborne transmission risks of both known and emerging infectious diseases, which are intensified by the growing capacity and density of modern passenger ships, while acknowledging that other mechanisms may also contribute to disease transmission. Hence, early risk assessment (RA) of disease transmissibility is essential for safeguarding public health and enhancing the passenger experience, preparing the cruise industry for future pandemics, and strengthening the overall resilience and safety of cruise operations. Fuzzy Cognitive Maps (FCMs) offer a valuable method for modeling complex data-driven systems in the context of risk assessment. However, traditional FCM construction is typically performed manually, which limits automation and hampers the accurate representation of uncertainty. We propose Intuitionistic Risk Assessment FCM (IRA-FCM), a novel framework that: (i) employs a hybrid learning approach that integrates unsupervised clustering to reveal hidden patterns within the data with supervised learning based on labeled instances to automatically learn the structure of an intuitionistic FCM; (ii) integrates multi-source sensor and system data with varying uncertainty levels; and (iii) models uncertainty via hesitancy, enabling more accurate, uncertainty-aware transmission risk assessment. Additionally, it estimates the confidence levels associated with various degrees of risk, serving as a comprehensive decision-support tool to ensure safety throughout the cruise duration by quantifying the uncertainty in its assessments. The effectiveness of the proposed framework is demonstrated on a dataset representing various airborne and close contact transmission scenarios of SARS-COV-2 within monitored areas, created using a validated agent-based model designed for airborne disease spread. The results validate its capacity to determine the transmission risk with an average accuracy of 88.6%. The applicability of the proposed framework extends beyond cruise ships, to assess the airborne disease transmission risk in ventilated indoor spaces with resident populations, such as apartment buildings, hotels and hospitals.

INDEX TERMS Risk assessment, fuzzy cognitive maps, interpretability, infectious diseases.

I. INTRODUCTION

Cruise tourism is experiencing rapid growth as it can provide a popular leisure holiday venue, with the number of cruise passengers projected to steadily increase [1]. However, the high population density, enclosed environments, and shared ventilation systems on cruise ships can create ideal conditions for the rapid spread of infectious diseases among passengers [2]. The transmission among ship passengers and crew became a major concern during the SARS-COV-2

The associate editor coordinating the review of this manuscript and approving it for publication was Ali Kashif Bashir.

pandemic, with cases and outbreaks reported on many cruise ships. The SARS-COV-2 virus can predominantly spread through airborne transmission and to a lesser extend through fomites [3]. Airborne transmission of infectious diseases may occur when viral particles, are expelled into the air through coughing, sneezing, or even talking [4], [5]. In indoor environments, such as the environments within a cruise ship, these droplets may remain suspended in the air for extended periods, especially in poorly ventilated areas, increasing the risk of exposure to nearby individuals [6]. The rapid transmission of airborne pathogens in ventilated maritime environments presents a significant challenge, especially with diseases like SARS-COV-2 due to its potential for asymptomatic spread and delayed detection. However, research on aerosol exposure and ventilation in specific shipboard microenvironments like restaurants and cabins remains notably limited [1]. Airborne diseases, including SARS-COV-2 and influenza, disseminate through respiratory droplets and aerosols that can persist in the air and travel widely via diffusion, convection, and ventilation systems; this risk is heightened by insufficient ventilation and prolonged exposure durations in shared spaces [7], [8], [9], [10]. This challenge is further compounded by the unique shipboard indoor environment, which, unlike land-based or air-based transportation, integrates work, living, and leisure within semi-enclosed spaces where crew members reside for extended periods, exposing them to pollutants from various sources like occupant activities, propulsion systems, and finishing materials [1].

Monitoring and controlling disease spread on cruise ships is crucial for enhancing passenger experience, preparing for future pandemics like SARS-COV-2 and influenza, and ultimately improving industry resilience and safety. This involves a multi-faceted approach: continuously monitoring ventilation conditions and aerosol dispersion to link them with airborne transmission risk, utilizing aerosol and ventilation performance data as input for computational fluid dynamics (CFD) simulations, and then modeling airborne disease transmission risk in controlled passenger ship environments. Several guidelines and protocols exist to manage health on vessels [2], but their effectiveness largely hinges on crew decisions and interventions. This reliance on human action makes on-board crisis management, especially during an epidemic, susceptible to human errors, which can be life-threatening for severe infectious diseases. The likelihood of such errors varies with factors like crew size, training, experience, vessel dimensions, and passenger numbers. Therefore, an automatic risk assessment method for disease spread monitoring and control on cruise ships is essential. An automatic, sensor-based system capable of detecting disease symptoms in the ship's indoor areas could effectively monitor and control disease spread, it would significantly reduce dependency on the human factor, thereby enhancing passenger safety [1], [2], [11], [12], [13].

Risk assessment (RA) methods for airborne disease transmission in ventilated indoor environments have primarily relied on epidemiological modeling, knowledge-based approaches, and probabilistic methods. Many studies have focused on long-term epidemic modeling to predict infection trends over days or weeks [14], [15], [16]. The World Health Organization (WHO) has also developed RA frameworks for pandemic outbreaks based on expert-driven methodologies [17]. However, these methods often lack adaptability to real-time conditions and emerging pathogens. Knowledge-based and probabilistic approaches have been widely applied in RA for disease transmission in ventilated indoor environments, particularly on cruise ships. These methods generally rely on evidence-based risk factors, such as overcrowding, poor ventilation, port visitation, pathogen concentration, and passenger exposure [7], [18], [19], [20]. Probabilistic models can provide valuable long-term risk estimations, but most existing methods focus on infection spread over multiple days [16] or lack temporal considerations altogether [7].

To overcome these challenges, smart sensor technologies have been explored to enhance epidemic monitoring and risk assessment. In accord with a recently conceptualized smart ship design this study proposes the integration of several smart sensors to the ship's infrastructure for detecting early signs of disease outbreaks. These include thermal cameras, which identify passengers with elevated facial temperatures [21], [22], [23] and audio sensors, such as microphones, to detect coughing in public spaces [24], [25], [26]. Air quality sensors embedded in the Heating, Ventilation, and Air Conditioning (HVAC) system that can monitor airborne pathogens, are still at prototype level [27], while personalized RFID sensors provide real-time occupancy tracking and passenger movement data, offering additional insights into potential transmission pathways. The fusion of sensor-based data with data from the ship's information system (SIS) provides a comprehensive, real-time framework for epidemic monitoring, allowing for automated risk assessment and decision support in high-density environments.

Soft computing techniques offer robust solutions for complex scientific challenges. Among these, Fuzzy Cognitive Maps (FCMs) stand out as graph knowledge-based methods, defining concepts and their causal relationships [28]. FCMs extend fuzzy logic by integrating causal links between risk factors, making them highly effective for modeling complex systems [29], [30], [31], [32], [33]. They've proven effective in epidemic risk assessments, especially at a national level, by combining expert knowledge with data-driven approaches to improve decision-making amidst uncertainty [34]. For instance, study [30] employed a hybrid-statistical advanced-fuzzy-cognitive-map algorithm to predict SARS-COV-2 cases using data from different countries.

Several modifications of FCMs have been proposed over the years aimed at overcoming limitations like potential biases introduced by experts during graph structure definition, which can compromise model accuracy [35]. Recognizing the inherent hesitation experts might have in precisely defining relations among graph concepts, researchers introduced intuitionistic FCM-I (iFCM-I) and intuitionistic FCM-II (iFCM-II) [36], [37]. These advanced models leverage intuitionistic fuzzy sets (IFSs) to effectively manage uncertainty, leading to more robust decision-making performance than their conventional counterparts. A key advantage is their built-in mechanism for assessing output quality via hesitancy estimation. Despite these compelling benefits, iFCMs have had limited practical applications to date, mainly in areas such as pneumonia severity assessment [36], chemical process control [37], time series forecasting [38], and celiac disease prediction [39].

In this paper, we introduce a novel framework based on iFCM-II called Intuitionistic Risk Assessment FCM (IRA-FCM). The key contributions of this framework are:

- A novel intuitionistic FCM that automates its structural definition using a supervised process, reducing manual intervention and potential biases.
- Capability to integrate multi-source information encompassing different levels of uncertainty from different sensors and the ship's information system, which is a critical step towards an essential smart ship functionality.
- Comprehensive uncertainty modeling through the intuitionistic concept of hesitancy, which enables a more accurate, uncertainty-informed method for assessing transmission risk.

The proposed framework provides estimations of confidence levels associated with various risk degrees. This capability positions it as a comprehensive decision-support tool, ensuring safety throughout the duration of a cruise by quantitatively assessing uncertainty in its evaluations. To the best of our knowledge this is the first data-driven risk assessment framework for disease transmission based on data from multiple sensors, and aims to cover the gap in the early prevention of disease spread in ventilated indoor spaces.

The rest of the paper is organized into five sections. Section II includes preliminaries. The proposed framework is presented in section III. Section IV presents the results of the experimental study demonstrating its effectiveness. Finally, concluding remarks and future work are summarized in the last section.

II. PRELIMINARIES

A. FUZZY COGNITIVE MAPS

Fuzzy Cognitive Maps (FCMs) are powerful tools for modeling complex systems. They are graph-based, knowledge-driven models consisting of nodes that represent system concepts and weighted edges that encode the causal relationships among these concepts. An FCM is formally defined as a directed graph comprising N concepts C_i, $i = 1, .., N$ and a set of weighted connections $w_{ji} \in [-1, 1]$, representing the strength and direction of influence from concept $C_i$to concept C_j [28]. Each of the N concepts C_i, $i = 1, \ldots, N$, of the FCM has a value $A_i \epsilon$ [0, 1]. There are three types of causal relationships: a) positive ($w_{ji} > 0$), which means that an increase in the value of C_j, causes an increase of the value of C_i, b) negative ($w_{ji} < 0$), indicating that increase in the value of C_j, causes a decrease of the value of C_i, and c) neutral $\left(w_{ji} = 0\right)$, meaning that there is no relationship between C_j and C_i. The construction of a Fuzzy Cognitive Map (FCM) involves the manual definition of a set of concepts and their corresponding weighted interconnections, a process that is guided by the expertise of domain specialists. Following the construction of the graph, a reasoning phase is initiated using a specific test case and proceeds iteratively until the FCM converges to a steady state. The values of the output concepts at this steady state are interpreted as the system's inferred outcomes. During this reasoning process, the concept activation values $A_i \epsilon$ [0, 1] are updated iteratively according to the following formulation:

$$A_i^{t+1} = \mathscr{f}\left(A_i^t + \sum\nolimits_{j=1, j\neq i}^{N} A_j^t \cdot w_{ji}\right) \tag{1}$$

where A_i^{t+1} represents the value of C_i at the iteration $t + 1$, w_{ji} is the influence of C_j on C_i, and $\mathscr{f}$ is a sigmoid function such as the log sigmoid, which maps the concept values within [0, 1] [40].

$$\mathscr{f}(x) = \frac{1}{1 + \exp(-x)} \tag{2}$$

The initial state vector A^0 represents the initial concept values, for $t = 0$.

B. INTUITIONISTIC FUZZY COGNITIVE MAPS

Intuitionistic fuzzy sets (IFSs) [41] extend the classical fuzzy set framework by incorporating a degree of non-membership that is independent of the membership degree, rather than being its complement. Given a universe of discourse G, an IFS is formally defined as follows

$$\mathcal{R} = \{\langle x, \mu_{\mathcal{R}}(x), \gamma_{\mathcal{R}}(x)\rangle \,|\, x \epsilon G\} \tag{3}$$

where $\mu_{\mathcal{R}}(x) \in [0, 1]$ and $\gamma_{\mathcal{R}}(x) \in [0, 1]$ define the degree of membership and non-membership, respectively of $x \in G$ to $\mathcal{R} \subset G$. The hesitancy $h_{\mathcal{R}}(x)$ of an element $x \in G$ to $\mathcal{S} \subset G$ is defined as follows:

$$h_{\mathcal{R}}(x) = 1 - \mu_{\mathcal{R}}(x) - \gamma_{\mathcal{R}}(x) \tag{4}$$

characterizing the indeterminacy (uncertainty) of the membership of x in $\mathcal{R}$.

iFCM-II [37] was proposed as an extension of the original FCM model, utilizing Intuitionistic Fuzzy Sets (IFSs) to effectively represent uncertainty, both in determining concept values and in assigning connection weights. An illustrative example of the iFCM-II model is shown in Fig. 1, where IFSs are depicted using simplified notation as $\{\langle v^{\mu}, v^{\gamma}\rangle\}_i$, $i = 1, \ldots, N$ and $\{\langle w^{\mu}, w^{\gamma}\rangle\}_{ji}, j = 1, \ldots, N$.

Uncertainty is captured through the hesitation degree inherent in IFSs, reflecting the natural indecisiveness that often characterizes human decision-making processes. Given a constructed iFCM-II model with specified weight pairs $\langle w^{\mu}, w^{\gamma}\rangle$, the reasoning process is carried out by iteratively computing the value pairs $\langle v^{\mu}, v^{\gamma}\rangle$ for each concept C_i,

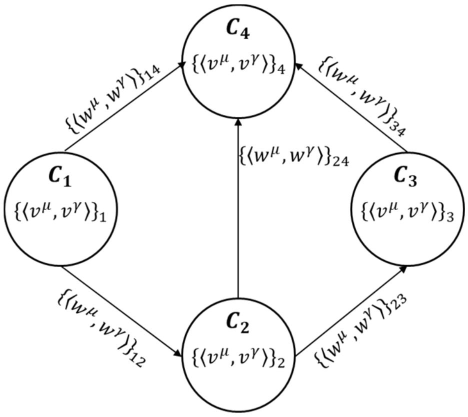

FIGURE 1. An example of a four-concept iFCM-II model.

$i = 1, \ldots, N$ using the following equation, which recursively updates the corresponding IFSs:

$$\{\langle v^\mu,\ v^\gamma\rangle\}_i^{t+1} = F\left(\{\langle v^\mu,\ v^\gamma\rangle\}_{\mathrm{i}}^{t} \oplus \left(\oplus_{\substack{j=1\\ j\neq i}}^{N}\left(\{\langle v^\mu,\ v^\gamma\rangle\}_j^{t} \otimes \{\langle w^\mu,\ w^\gamma\rangle\}_{ji}^{t}\right)\right)\right) \tag{5}$$

where the symbols "⊕" and "⊗", correspond to the summation and multiplication operators, respectively and $F(\mathcal{R}) = \{\langle \not{f}_\mu,\ \not{f}_\gamma\rangle\}$ are transformation functions defined on IFSs.

As proved in [37], a pair $\langle v^\mu,\ v^\gamma\rangle$ from $\{\langle v^\mu,\ v^\gamma\rangle\}_i^{t+1}$ is calculated as follows:

$$\left(v_i^\mu\right)^{t+1} = \not{f}_\mu\left(\left(v_i^\mu + \left(1 - v_i^\mu\right)\cdot\sigma_{iN}\right)^t\right) \tag{6}$$

$$\left(v_i^\gamma\right)^{t+1} = \not{f}_\gamma\left(\left(v_i^\gamma \cdot \prod_{j=1,\ j\neq i}^{N}\left(v_j^\gamma + w_{ji}^\gamma - v_j^\gamma w_{ji}^\gamma\right)\right)^t\right) \tag{7}$$

where $\left(v_i^\mu\right)^{t+1}$ and $\left(v_i^\gamma\right)^{t+1}$ represent the membership and non-membership of C_i, respectively, at iteration $_t + 1$, and the calculation of $_{\sigma_{iN}}$ is performed by

$$\sigma_{ij} = \begin{cases} v_1^\mu \cdot w_{1i}^\mu, & j = 1 \\ \sigma_{i(j-1)} + v_j^\mu \cdot w_{ji}^\mu - \sigma_{i(j-1)} \cdot v_j^\mu \cdot w_{ji}^\mu, & j > 1 \end{cases} \tag{8}$$

The variables w_{ji}^μ and w_{ji}^γ represent the membership and non-membership, respectively, of the weights corresponding to the arcs directed from node j to node i. The real hesitancy $(\hbar_i)$ of a concept C_i is given by (9):

$$\hbar_i = 1 - \not{f}_\mu^{-1}\left(v_i^\mu\right) - \not{f}_\gamma^{-1}\left(v_i^\gamma\right) \tag{9}$$

where $F^{-1}(S) = \left\{\left\langle \not{f}_\mu^{-1},\ \not{f}_\gamma^{-1}\right\rangle\right\}$ represents the inverse of function $F(S)$, and $_{\not{f}_\mu^{-1}}\left(v_i^\mu\right)$ and $_{\not{f}_\gamma^{-1}}\left(v_i^\gamma\right)$, considering $\not{f}^{-1}$ to be the inverse of $\not{f}$, represent the real membership and non-membership values of that concept.

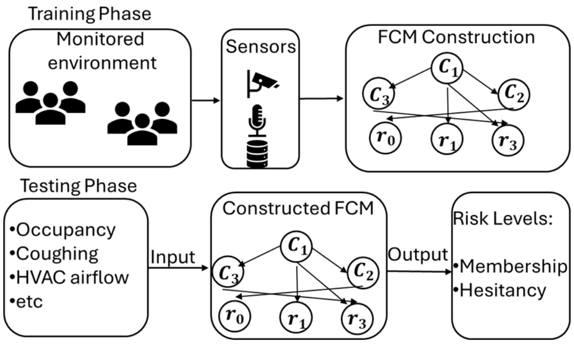

FIGURE 2. Overview of the proposed framework.

III. METHODOLOGY

The proposed risk assessment framework consists of two main phases: training, described in Algorithm 1, and testing (Fig. 2). During the training phase, data related to each risk factor are obtained from simulated scenarios representing different shipboard environments such as cabins, lounges, and restaurants. Each scenario includes one or more infectious individuals exhibiting symptoms consistent with COVID-19 (e.g., coughing), among other passengers. These symptoms are detectable by sensors installed in the monitored spaces, which do not identify specific individuals but indicate the presence of infection risk within the area. Both the symptoms and their detection by the sensors are simulated, considering a detection accuracy in line with recent studies (microphone 97% [25], fever detection 96% [21]). Then, an agent-based model (ABM) determines the resulting number of secondary infections. This outcome provides information about the transmission risk. The corresponding risk factors, such as occupancy, exposure time, and airflow conditions, are then mapped to linguistically expressed risk states (labels) represented by fuzzy sets. In this way, the IRA-FCM is trained on labeled datasets that capture realistic transmission dynamics.

Data sources include RFID sensors tracking the number of occupants within the monitored environment, thermal cameras assessing the facial temperature of the passengers, audio sensors monitoring sounds related to symptoms, *e.g.*, coughing. This data is labeled using fuzzy sets to represent the uncertainty associated with each risk level. The resulting dataset is then used to automatically construct the IRA-FCM model. The construction of the IRA-FCM involves identifying input and output concepts and automatically calculating the weights between them based on the training data. As a data-driven approach, the proposed IRA-FCM framework is adaptable to any type of monitoring environment, such as smart ships.

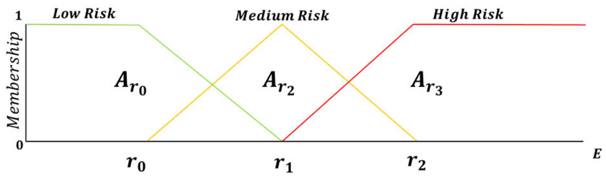

FIGURE 3. Multi-source data risk labeling.

In the testing phase (Fig. 2), the trained IRA-FCM model generates risk assessment recommendations, using the data collected during a ship's journey. It evaluates the safety level by continuously assessing the input values through fuzzy reasoning sessions. Each reasoning session converges to a steady state indicating the risk levels via the respective membership values and the hesitancy associated with these levels, which characterizes the non-confidence of the respective membership estimation. Therefore, the confidence of a predicted risk can be obtained as one minus hesitancy. Throughout this process, the framework also provides explanations for its decisions, fostering user trust.

A. FEATURE EXTRACTION

To evaluate infection risk, relevant factors associated with each data stream must be defined. For instance, this study focuses on estimating exposure to pathogen load of a person, which can be translated into infection probability using dose-response models [12]. While simple models, such as exponential relationships, are commonly employed, their calibration remains difficult due to uncertainties in key parameters, including the median infective dose of SARS-CoV-2, which may vary by host, viral variant, and transmission route [12]. Infectious individuals exhale pathogens bound to aerosols, while susceptible individuals may inhale these particles when passing through contaminated air. The pathogen load within an aerosol cloud varies over time, directly influencing transmission risk. Current estimates suggest that infection may require inhalation of 10^2 to 10^3 viral particles [12], though lower doses may also suffice. Considering the uncertainty with respect to fuzzy set-based approach is adopted, where individuals inhaling pathogen between automatic calculated fuzzy set loads can be classified as 'high/medium/low risk.'

The first step of the methodology involves constructing appropriate fuzzy sets that linguistically characterize the universe of discourse E under consideration, *e.g.*, inhalation of pathogen from an individual. The universe of discourse is uniformly divided in R segments (risk levels) and each segment $r \in [0, R]$ is characterized by a fuzzy set A_r. Fig. 2 illustrates an example where the universe E is uniformly divided in three segments r_0, r_1, r_2. Each segment is associated with one of the fuzzy sets $A_{r_0}, A_{r_1}, A_{r_2}$, each of which denotes a different linguistically expressed risk level and is characterized by a membership functionμ_{r_R}. For instance, A_{r_0} is labeled as "Low" and A_{r_2} as "High", thereby representing a spectrum of infection risk from low to high.

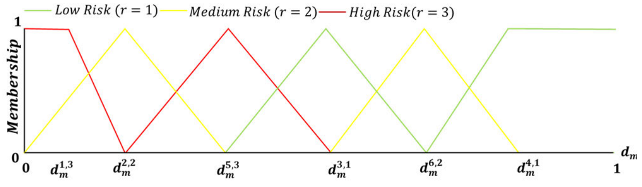

FIGURE 4. Linguistic description of a feature, e.g., of a risk factor.

The second step of the methodology involves data collection, feature extraction, and data labeling according to risk levels. Let us consider a set of K different cases, each involving M different sensors. Each case can be described by a feature vector $\boldsymbol{x}_k = (x_1, \ldots, x_M), k = 1, \ldots, K$, and the feature components x_m capture multi-source data information from M sensors. Each feature vector $\boldsymbol{x}_k$ is associated with a value $e_k \in E$, such as the estimated mean inhalation of pathogens by individuals in the monitored environment. Based on e_k each $\boldsymbol{x}_k$is associated with a ground-truth class vectors $\mathbf{y_k} = [\mu_1(e_k), \mu_2(e_k), \ \ldots \mu_R(e_k)]$, where R denotes the total number of risk levels in the training dataset and $\mu_r(e_k)$ is associated with a membership degree to each fuzzy set A_r corresponding to a risk level r.

B. LINGUISTIC DESCRIPTION OF FEATURES

The third step of the proposed methodology aims to linguistically characterize every feature x_m of each feature vector $\boldsymbol{x}_k$ using fuzzy sets. To facilitate consistent fuzzy set operations, all training feature vectors are first normalized to the range [0, 1], ensuring a common universe of discourse across all features. Next, the feature vectors are grouped into C clusters using a clustering algorithm, such as $k-$means. Each cluster is then associated with a specific risk level, determined by the most frequently occurring class within that cluster. The purpose of this clustering step is to capture the relationship between each feature and the corresponding risk level. Let $\boldsymbol{d_{c,r}} = \left(d_1^{c,r}, \ldots, d_M^{c,r}\right),\ c = 1, \ldots, C$ be the cluster centers corresponding to risk level r. Each component $d_m^{c,r}$ represents the mean value of the multi-source data collected from the M sensors within cluster c. For each component $d_m^{c,r}$ a corresponding fuzzy set $A_{d_m^{c,r}}$ is defined. This set is characterized by a membership function $\mu_{d_m^{c,r}}(x_m) \in [0, 1]$, which for simplicity is considered triangular. The top of this triangular function is positioned at $d_m^{c,r}$ and its base extends to the nearest neighboring component $d_m^{c',r'}$, $c \neq c'$, $r \neq r'$ or to the boundary values 0 or 1 using trapezoidal membership function, depending on which is closest. An illustrative example of the definition of fuzzy sets $A_{d_m^{c,r}}$ is presented in Fig. 4, where the number of clusters is $C = 6$ and the number of risk levels is $R = 3$. In this figure the risk level associated with each component is characterized is by linguistic values from "Low" to "High" and it is visualized using different colors corresponding to the identified risk levels.

Intuitionistic fuzzy sets are modeled using both membership and non-membership functions. The membership function defined previously $\mu_{d_m^{c,r}}(x_m) \in [0, 1]$ represents the degree to which a feature d_m belongs to a specific risk level. The corresponding non-membership function $\gamma_{d_m^{c,r}}(x_m) \in [0, 1]$ expresses the membership of feature d_m to the other risk levels. Following the approach described in [37], the subset of pairs of fuzzy sets from $A_{d_m^{c,r}} \times A_{d_m^{c',r'}}$ where $\forall c' \neq c, \forall r' \neq r$ that satisfy the conditions imposed by the definition of an IFS (section II.B) are consider as pairs of membership and non-membership functions, generating a set

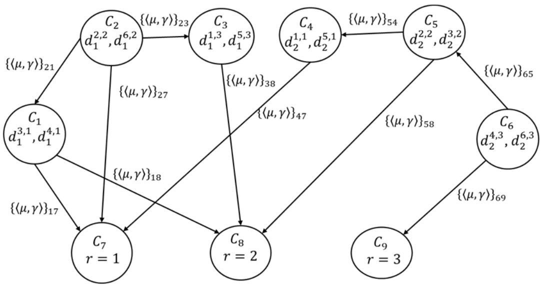

FIGURE 5. IRA-FCM example model.

of IFSs $B^n_{d_m^{c,r}}$

$$B^n_{d_m^{c,r}} = \{x_m, \mu_{d_m^{c,r}}(x_m), \gamma_{d_m^{c',r'}}(x_m) \,|x_m \in [0,1]\} \tag{10}$$

where $n = 1, \ldots, N$ and N is the number of different generated IFSs.

C. AUTOMATIC IRA-FCM CONSTRUCTION

The fourth step of the methodology is associated with the construction of IRA-FCM models. Unlike traditional FCMs, which rely on expert input, the proposed framework is fully data-driven. It automatically determines the structure of the models and computes the weights of the interconnections based on the training data.

In the FCM graph of IRA-FCM model, the input nodes represent the various risk levels associated with each feature x_m, while the output nodes correspond to the overall risk levels. Fig. 5 illustrates IRA-FCM model defined using the proposed framework. Each input concept is associated with a $d_m^{c,r}, m = 1, \ldots, M, \ r = 1, \ldots, R$. The model includes six input concepts, *i.e.*, $C_1 - C_6$ corresponding to $M = 2$ features, $C = 6$ clusters and $R = 3$ risk levels. Thus, there are three output concepts, one for each risk level. In each node of Fig. 5, the corresponding $d_m^{c,r}$ values for each input node and the risk levels for each output node is presented.

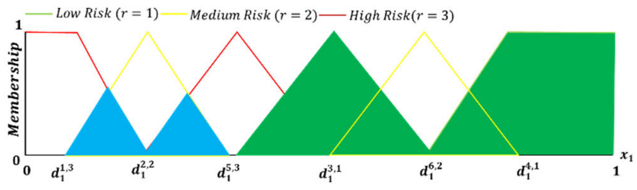

FIGURE 6. Intuitionistic Fuzzy Union and Intuitionistic Intersection for the computation of $w_{1,7}, \{\langle\mu,\gamma\rangle\}_{1,7}$.

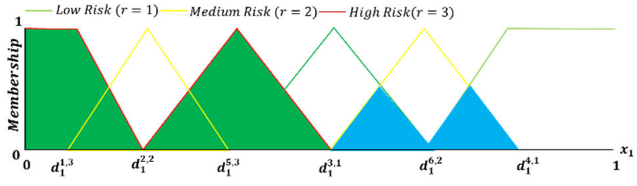

FIGURE 7. Intuitionistic Fuzzy Intersection and Intuitionistic Union for the computation of $w_{2,1}, \{\langle\mu,\gamma\rangle\}_{2,1}$.

The influence between any two connected concepts C_i and C_j, $i \neq j$ of the IRA-FCM is expressed by an IFS of the form $\{\langle \mu_{d_m^{c,r}}, \gamma_{d_m^{c,r}} \rangle\}_{j,i}$. Two types of relations are considered within the model: a) connections between the input and output concepts, and b) connections between the input concepts.

The relationships between the input and output concepts are defined and linguistically characterized to represent the influence between these concepts $B_{j,i} = \left\{\left\langle \mu_{d_m^{c,r}}, \gamma_{d_m^{c',r'}} \right\rangle\right\}_{j,i}$ are constructed as follows:

$$B_{j,i} = \cup_{n=1}^{N} B^n_{d_m^{c,r}} \tag{11}$$

The symbol "∪" represents the intuitionistic fuzzy union operation performed between concepts C_i and C_j, $i \neq j$. Fig. 6 illustrates the intuitionistic fuzzy set union for the linguistic characterization of input-output relation between the nodes C_1 and C_7. The result of the union is the fuzzy set that is filled with green color and has a membership $\mu_{d_m^{c,r}}$. The result of the intersection is represented with blue color and has a non-membership $\gamma_{d_m^{c,r}}$.

The relationships between the input concepts are defined as follows:

$$B_{j,i} = \left(\cup_{n=1}^{N} B^n_{d_m^{c,r}}\right) \cap \left(\cup_{n=1}^{N} B^n_{d_{m'}^{c,r}}\right) \tag{12}$$

where $m \neq m', m, m' = 1, \ldots, M, i \neq j$. The symbol "∩" represents the intuitionistic fuzzy intersection operation performed between concepts C_i and C_j, $i \neq j$. Fig. 7 illustrates the intuitionistic fuzzy set intersection for the linguistic characterization of the input-input relation of node C_1 and C_2. The result of the intersection is the fuzzy set that is filled with blue color and has a membership $\mu_{d_m^{c,r}}$. The result of the union is represented with green color and corresponds to a non-membership $\gamma_{d_m^{c,r}}$.

The use of the fuzzy union operation reflects the process involved in constructing an FCM or an iFCM, where inputs from multiple experts are aggregated to define and model the relationships among various factors in a given problem. In this context, experts' consensus regarding the strength or existence of these relationships is captured using the fuzzy intersection operation. In all the afore-mentioned cases, the interconnection weights between concepts C_i and C_j, $i \neq j$ are calculated using the center of gravity of the fuzzy sets for FCM and the intuitionistic center of area (ICOA) of each $B_{j,i}$ [42].

D. TESTING PHASE

Given a test input feature vector composed of the data from various sensors $\boldsymbol{x} = (x_1, \ldots, x_M)$. The membership and non-membership for each feature x_m is computed. The result is the state vector with linguistic description for each x_m for IRA-FCM that has the form

$$\begin{aligned} \boldsymbol{A} = (& \left\langle \mu_{d_1^{c,1}}(x_1), \gamma_{d_1^{c,1}}(x_1) \right\rangle, \ldots, \left\langle \mu_{d_1^{c,R}}(x_1), \gamma_{d_1^{c,r}}(x_1) \right\rangle \\ & , \ldots, \left\langle \mu_{d_M^{c,R}}(x_M), \gamma_{d_M^{c,R}}(x_M) \right\rangle) \end{aligned} \tag{13}$$

The reasoning process is then performed by iteratively calculating the pairs $\langle \mu_{d_m^{c,r}}, \gamma_{d_m^{c,r}} \rangle$, where each output represents

Algorithm 1 IRA-FCM Training

```
Input: Multi-source sensor data, Number of clusters $C$, Risk levels
    $R$, Intuitionistic fuzzy set definitions.
Output: Weight matrix $W$.
// Feature Extraction
Collect multi-source sensor data from monitored environments;
Construct feature vectors $\boldsymbol{x}_k = (x_1, \ldots, x_M), k = 1, \ldots, K$;
Estimate the mean pathogen inhalation $e_k \in E$ from simulations;
Assign ground-truth fuzzy risk labels
    $\boldsymbol{y_k} = [\mu_1(e_k), \mu_2(e_k), \ldots \mu_R(e_k)]$;
//Linguistic Feature Description
Normalize all feature vectors to [0, 1];
Cluster normalized features $\boldsymbol{x}_k$ into $C$ groups;
Assign each cluster to the most frequent risk level;
For each cluster center $\mathbf{d_{c,r}} = (d_1^{c,r}, \ldots, d_M^{c,r})$, $c = 1, \ldots, C$ do:
    Define triangular/trapezoidal membership functions;
    Construct intuitionistic fuzzy sets based on Eq. (10);
//Automatic IRA-FCM Construction
Define Concepts:
    Input nodes = feature clusters $d_m^{c,r}$;
    Output nodes = overall risk levels $R$;
// Weight Learning
For each input–output pair $(C_i, C_j)$, $i \neq j$:
    Compute intuitionistic fuzzy union using Eq. (11);
For each input–input pair $(C_i, C_j)$, $i \neq j$:
    Compute intuitionistic fuzzy intersection using Eq. (12);
For each other pair $(C_i, C_j)$, $i \neq j$:
    Compute interconnection weights $w_{i,j} = \mathrm{ICOA}(B_{j,i})$;
Store all $w_{i,j}$ in weight matrix $W$;
```

a degree of association with risk levels corresponding to the input test feature vector.

IV. EXPERIMENTAL STUDY

A. DATASET CREATION AND PARAMETER SETTINGS

Since datasets for short-term disease transmission in the shipboard scenarios examined are not available, a validated ABM capable of airborne disease transmission [12] was utilized to simulate such scenarios. This ABM serves as a surrogate, enabling the controlled generation of simulated outbreak scenarios across diverse ship environments with varying risk factors such as ventilation rates and occupancy. Each ABM simulation produces outcomes in terms of secondary infections, allowing the training process to capture realistic epidemiological dynamics, while addressing the data limitations.

By utilizing the aforementioned ABM, a dataset was developed to assess the effectiveness of the proposed framework and to demonstrate its applicability to disease transmission on board cruise ships. The dataset included various distinct SARS-COV-2 transmission scenarios that were simulated across eight monitored shipboard areas.

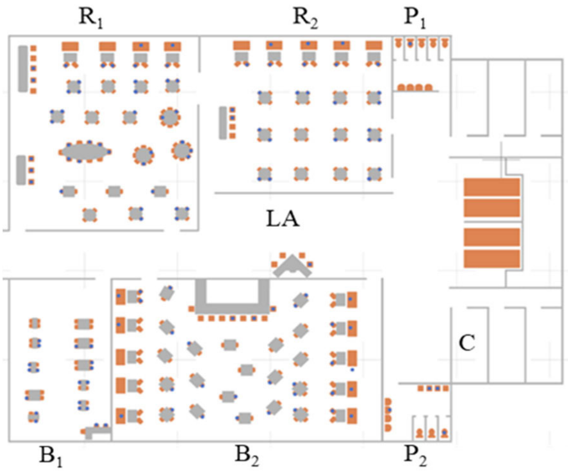

FIGURE 8. ABM-simulated monitored environment.

In each simulated scenario, a group of passengers was placed in a designated area, including a single infectious individual exhibiting symptoms consistent with COVID-19 (e.g., coughing), which are detectable by sensors installed in the monitored space. These sensors do not identify specific individuals but only detect the presence of symptoms within the room. Therefore, the system assumes the presence of an infectious case based on symptom detection. Subsequently, the rest of the passengers in the simulation were considered susceptible, *i.e.*, healthy individuals capable of contracting the disease.

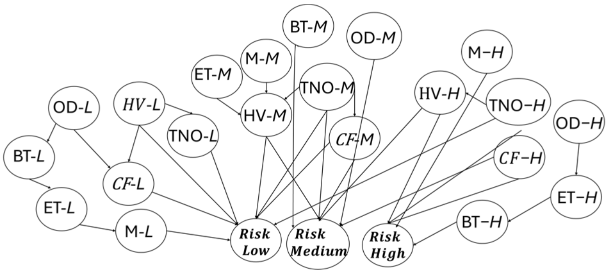

FIGURE 9. IRA-FCM structure for infectious disease transmission risk assessment in cruise ships.

Simulations were then conducted, allowing passengers to interact randomly over a set period to assess the exposure levels of healthy individuals. The number of newly infected passengers was subsequently determined based on the simulation outcomes. The risk was determined based on the average absorbed pathogen load. This number was then used to determine the level of risk R of SARS-COV-2 transmission for each simulation.

To capture the variability in population density and room characteristics across different indoor spaces on a cruise ship, simulations were conducted for several representative areas. Specifically, five types of indoor environments were examined: restaurants, bars, lounge areas, public toilets, and private cabins. For each selected area on the representative cruise ship, detailed simulations were performed to analyze disease transmission dynamics under varying conditions. An example of monitored environment from ABM simulations is presented in Fig. 8. The characteristics of each monitored environment are provided in Table 1. The capacity of each area was defined based on its typical maximum occupancy during peak usage, using actual ship schematics and layout specifications. For seated areas such as restaurants and lounges, this corresponds to the number of available seats indicated in the ship's design plans. In contrast, the capacity of public toilets includes both individuals inside the facility and those queuing outside to emulate high-exposure scenarios during peak hours. This broader definition ensures that the transmission risk assessment captures realistic crowding conditions and potential exposure levels within these monitored areas.

ABM simulations were performed by allowing infected passengers to interact with each other, releasing pathogens primarily through coughing and, to a lesser extent, breathing. A total of 3,000 simulations were performed, spanning 300 simulations per area, with each scenario repeated 10 times to account for stochastic variability in passenger interactions.

The results demonstrated consistency, with an average standard deviation of approximately 300 across repeated simulations. To perform the RA of airborne disease spread, this work investigates the following risk factors which are data collected by sensors: maximum body temperature (BT), HVAC airflow (HV), exposure time (ET), total number of occupants (TNO) in a room, occupant distance (OD), passengers who wear mask (M), passenger who had been vaccinated (V), and coughing frequency (CF). The value ranges for each risk factor are HV = [0, 10170]m^3/h, BT = [36], [41]°C, ET = [15,120] min, TNO = [2,88], CF = [0, 650], OD = [0, 2] m, M = [0, 88], V = [0, 88]. A detailed mapping of risk factors with ABM parameters can be found in Table 2.

B. EXPERIMENTAL RESULTS

The results of the experiments are quantified in terms of accuracy and Mean Square Error (MSE). The accuracy quantifies the effectiveness of the framework to correctly predict the risk level and configure the overall risk assessment for different cases, based on their characteristics. The accuracy is calculated by the following equation

$$Accuracy = P/S \tag{14}$$

where P is the number of correctly predicted risk level and S is the number of total actual simulated risk levels for all the test cases. The MSE is calculated by the following equation

$$MSE = \frac{1}{R}\sum_{r=1}^{R}\left(\mu_r(e) - \mu'_r(e)\right)^2 \tag{15}$$

where $\mu_r(e)$, $\mu'_r(e)$, $r = 1 \ldots R$ correspond to the actual membership value and the predicted membership from IRA-FCM, where a monitored environment is considered. For the evaluation of the proposed method, we conducted a series of experiments using a leave-one-out cross-validation strategy for each monitoring environment. This evaluation strategy ensures robustness by iteratively testing each data point while training on the remainder. In addition, to assess cross-environment generalization, we adopted a leave-one-environment-out (LOEO) protocol, where the model is trained on data from all but one environment and then tested on the held-out environment. By rotating through all environments, the LOEO strategy provides a more rigorous evaluation of the method's ability to generalize across different conditions. To highlight the impact of intuitionistic fuzzy modeling the proposed IRA-FCM is compared to the conventional FCM where influence between any two connected concepts C_i and C_j, $i \neq j$ of the FCM is expressed by a fuzzy set. The respective FCM will be referred to as RA-FCM in the rest of this study.

TABLE 1. Indoor environments characteristics.

INDOOR ENVIRONMENTS	**Capacity**	**Surface Area**	**Volume (*V*)**
Restaurant 1 (R_1)	82	356 m^2	1068 m^3
Restaurant 2 (R_2)	42	264 m^2	792 m^3
Bar 1 (B_1)	44	197 m^2	591 m^3
Bar 2 (B_2)	88	413 m^2	1219 m^3
Lounge area (LA)	50	565 m^2	1695 m^3
Public toilet 1 (P_1)	15	36 m^2	108 m^3
Public toilet 2 (P_2)	20	42 m^2	126 m^3
Cabin (C)	6	32 m^2	96 m^3

The experimental investigation involves constructing multiple instances of the RA-FCM and IRA-FCM frameworks, tailored to different combinations of input and output concepts. The weights between these concepts are automatically learned from the training data, enabling a data-driven modeling approach based on sensor-collected information. This design allows the proposed RA-FCM and IRA-FCM frameworks to adapt flexibly to various monitoring environments. To evaluate the models, we examined three distinct sets of risk factors as inputs. The first set includes HV, TNO, OD, and CF; the second set includes HV, CF, M, and V; and the third set comprises all the aforementioned risk factors. The first set of risk factor is constructed in order to examine the relationship between the room ventilation when the number of persons and their distance changes [43], [44]. The second set of risk factor is considered in order to examine the relationship between the room ventilation changes and the persons who have been vaccinated and wears mask [45]. The third set of risk factors is considered in order to examine the performance of IRA-FCM using all the available risk factors. Fig. 9 illustrates a representative structure of the RA-FCM and IRA-FCM models, where the input concepts represent all relevant risk factors for each risk level $r = 1, .., R$ and the output concepts represent the risk levels. For each experiment, the clustering process was carried out using the k-means algorithm [46] with Euclidean distance, serving as a baseline clustering method. The optimal number of clusters was determined through grid search over a range of values from 3 to 50. The fuzzy sets were implemented using triangular membership functions. In the reasoning process sigmoid functions were utilized. The hesitancy values of the IRA-FCM concepts were initially set to 0.

The performance of the RA-FCM and IRA-FCM models for each set of risk factors is summarized in Tables 3–5,

TABLE 2. Correspondence of risk factors with ABM parameters.

Risk factors	ABM parameters
Coughing frequency	Number of coughs per minute
Occupancy	Occupants per m^2
Exposure Time	Simulation Time
Temperature	Temperature per occupant
Masks	Percentage of occupants wearing masks
Vaccination	Percentage of vaccinated occupants

where the mean values of accuracy and mean squared error (MSE) are reported. The standard deviation of the respective experiments was of the order of ±0.01. The highest accuracy scores and the lowest MSE values are highlighted in bold.

It can be observed that IRA-FCM consistently outperforms the RA-FCM in terms of average accuracy and MSE. Furthermore, the results presented in Tables 3 and 4 demonstrate higher accuracy compared to those in Table 5, suggesting that interdependencies among the risk factors may negatively impact classification performance when all factors are combined. The lower MSE values reported in Table 5 indicate greater uncertainty in the computation of membership values during the reasoning process when all risk factors are included. This increased uncertainty likely contributes to the observed decrease in accuracy. Additionally, these findings suggest a significant overlap between the fuzzy sets of the risk factors.

Furthermore, comparison with Logistic Regression (LR) was conducted with the same multi-source feature data used for IRA-FCM. The results are summarized in Tables 6, 7 and 8. It can be observed that across all indoor environments, IRA-FCM consistently achieves higher accuracy and lower MSE, reflecting its ability to capture complex, nonlinear relationships and uncertainty in multi-source sensor data.

TABLE 3. Results of RA-FCM and IRA-FCM using the first set of risk factors.

INDOOR ENVIRONMENTS	ACC RA-FCM	ACC IRA-FCM	MSE RA-FCM	MSE IRA-FCM
Restaurant 1 (R$_1$)	0.73	**0.78**	1.09	**0.90**
Restaurant 2 (R$_2$)	0.88	**0.92**	1.40	**1.22**
Bar 1 (B$_1$)	0.94	**0.96**	1.12	**1.09**
Bar 2 (B$_2$)	0.93	**0.94**	1.30	**1.13**
Lounge area (LA)	0.94	**0.99**	1.39	**1.20**
Public toilet 1 (P$_1$)	0.85	**0.94**	1.47	**1.22**
Public toilet 2 (P$_2$)	0.95	**0.98**	1.12	**0.97**
Cabin (C)	0.82	**0.88**	1.26	**1.11**
Average	0.88	**0.92**	1.16	**1.10**

Additional experiments were conducted following a LOEO protocol. The results of these experiments are presented in Tables 9 and 10, which summarize the performance of RA-FCM, IRA-FCM, and logistic regression across all held-out environments. These results provide a comprehensive assessment of the methods' cross-environment generalization, highlighting their robustness when deployed in previously unseen environments.

TABLE 4. Results of RA-FCM and IRA-FCM using the second set of risk factors.

INDOOR ENVIRONMENTS	ACC RA-FCM	ACC IRA-FCM	MSE RA-FCM	MSE IRA-FCM
Restaurant 1 (R$_1$)	0.80	**0.91**	1.08	**0.92**
Restaurant 2 (R$_2$)	0.96	**0.99**	1.35	**1.16**
Bar 1 (B$_1$)	0.89	**0.95**	1.40	**1.20**
Bar 2 (B$_2$)	0.97	**0.99**	1.16	**1.02**
Lounge area (LA)	0.73	**0.83**	1.59	**1.26**
Public toilet 1 (P$_1$)	0.88	**0.91**	1.11	**0.98**
Public toilet 2 (P$_2$)	**0.92**	0.88	**1.14**	1.19
Cabin (C)	0.82	**0.83**	1.29	**1.11**
Average	0.87	**0.91**	1.26	**1.11**

TABLE 5. Results of RA-FCM and IRA-FCM using the third set of risk factors.

INDOOR ENVIRONMENTS	ACC RA-FCM	ACC IRA-FCM	MSE RA-FCM	MSE IRA-FCM
Restaurant 1 (R$_1$)	0.82	**0.87**	0.22	**0.18**
Restaurant 2 (R$_2$)	0.80	**0.83**	0.25	**0.19**
Bar 1 (B$_1$)	0.93	**0.94**	0.23	**0.16**
Bar 2 (B$_2$)	0.82	**0.85**	0.22	**0.18**
Lounge area (LA)	0.84	**0.86**	0.20	**0.17**
Public toilet 1 (P$_1$)	0.70	**0.74**	0.32	**0.22**
Public toilet 2 (P$_2$)	0.79	**0.81**	0.21	**0.14**
Cabin (C)	0.76	**0.81**	0.19	**0.14**
Average	0.80	**0.83**	0.23	**0.17**

TABLE 6. Results of BAseline and IRA-FCM using the first set of risk factors.

INDOOR ENVIRONMENTS	ACC IRA-FCM	ACC LR	MSE IRA-FCM	MSE LR
Restaurant 1 (R$_1$)	**0.78**	0.72	**0.90**	1.15
Restaurant 2 (R$_2$)	**0.92**	0.87	**1.22**	1.40
Bar 1 (B$_1$)	**0.96**	0.90	**1.09**	1.28
Bar 2 (B$_2$)	**0.94**	0.89	**1.13**	1.31
Lounge area (LA)	**0.99**	0.85	**1.20**	1.50
Public toilet 1 (P$_1$)	**0.94**	0.88	**1.22**	1.33
Public toilet 2 (P$_2$)	**0.98**	0.91	**0.97**	1.10
Cabin (C)	**0.88**	0.82	**1.11**	1.27
Average	**0.92**	0.87	**1.10**	1.31

TABLE 7. Results of RA-FCM and IRA-FCM using the second set of risk factors.

INDOOR ENVIRONMENTS	ACC IRA-FCM	ACC LR	MSE IRA-FCM	MSE LR
Restaurant 1 (R$_1$)	**0.91**	0.85	**0.92**	1.10
Restaurant 2 (R$_2$)	**0.99**	0.93	**1.16**	1.32
Bar 1 (B$_1$)	**0.95**	0.88	**1.20**	1.35
Bar 2 (B$_2$)	**0.99**	0.92	**1.02**	1.18
Lounge area (LA)	**0.83**	0.76	**1.26**	1.50
Public toilet 1 (P$_1$)	**0.91**	0.84	**0.98**	1.12
Public toilet 2 (P$_2$)	0.88	0.80	**1.19**	1.38
Cabin (C)	**0.83**	0.78	**1.11**	1.28
Average	**0.91**	0.84	**1.11**	1.28

C. INTERPRETABILITY ANALYSIS

To better understand the proposed framework, an indicative risk assessment example, using the IRA-FCM, is presented in this subsection. Let us consider the monitoring environment

TABLE 8. Results of RA-FCM and IRA-FCM using the third set of risk factors.

INDOOR ENVIRONMENTS	ACC IRA-FCM	ACC LR	MSE IRA-FCM	MSE LR
Restaurant 1 (R_1)	**0.87**	0.80	**0.18**	0.25
Restaurant 2 (R_2)	**0.83**	0.77	**0.19**	0.28
Bar 1 (B_1)	**0.94**	0.88	**0.16**	0.22
Bar 2 (B_2)	**0.85**	0.78	**0.18**	0.25
Lounge area (LA)	**0.86**	0.79	**0.17**	0.24
Public toilet 1 (P_1)	**0.74**	0.68	**0.22**	0.30
Public toilet 2 (P_2)	**0.81**	0.74	**0.14**	0.21
Cabin (C)	**0.81**	0.76	**0.14**	0.20
Average	**0.83**	0.77	**0.17**	0.24

TABLE 9. Results of RA-FCM and IRA-FCM using LOEO.

RISK FACTORS SETS	ACC RA-FCM	ACC IRA-FCM	MSE RA-FCM	MSE IRA-FCM
First	0.65	**0.68**	1.01	**0.88**
Second	0.60	**0.66**	1.08	**0.90**
Third	0.58	**0.64**	0.98	**0.91**

TABLE 10. Results of LR and IRA-FCM using LOEO.

RISK FACTORS SETS	ACC LR-FCM	ACC IRA-FCM	MSE LR-FCM	MSE IRA-FCM
First	0.57	**0.68**	0.96	**0.88**
Second	0.54	**0.66**	0.92	**0.90**
Third	0.46	**0.64**	1.08	**0.91**

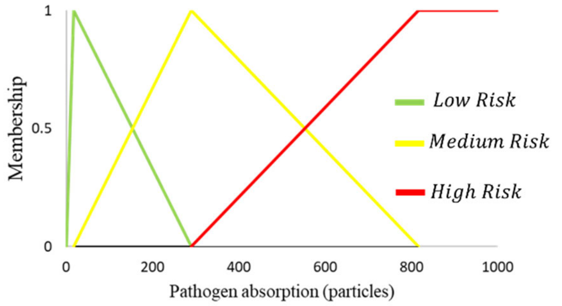

FIGURE 10. Corresponding risk levels derived from previous simulation data.

of a cruise restaurant, where the maximum number of passengers is 88 and the airflow rate that defines the number of air changes per hour and the volume of the examined area (m^3) is 2786 m^3/h. The number of passengers is 35, from them 20 wear masks and 8 are vaccinated. The passengers spend 79 minutes in the restaurant with an average contact distance of 0.37m. The number of coughs that have been counted per minute is 85. Based on the simulation data of the same room under varying conditions, the estimated absorption of pathogen particles is calculated for each individual [12]. The number of pathogens accumulated by a person describes the person's degree of exposure. This degree of exposure can be translated into a risk level. In this example, the risk levels are automatically computed from the simulations, and they are linguistically described using fuzzy sets, as it is described in section III-A. Figure 10 illustrates the computed fuzzy sets (section III-A) and corresponding risk levels derived from previous simulation data. Unlike crisp thresholds, fuzzy sets allow for gradual transitions between categories: for example, the red curve for high risk begins to rise below 300 particles, indicating partial membership in that category, while full membership is only reached at higher absorption levels. The results indicate that a high risk of infection from SARS-Cov-2 begins at an absorption level of approximately 800 particles, which closely aligns with the 1000-particle threshold identified in the study as the exposure level for infection [12]. Then the rest of the fuzzy sets that describe the characteristics of the monitored environment are computed based on the sections III-B and III-C.

For this example, we use the constructed RA-FCM and IRA FCM which uses the second set of risk factors that include HV, CF, M, and V. According to the subjection III-D the initial state vector for the monitored environment is

$$\begin{aligned}
A_{RA-FCM} &= (C_1, C_2, C_3, C_4, C_5, C_6, C_7, C_8, C_9, C_{10}, \\
&\quad C_{11}, C_{12}, C_{13}, C_{14}, C_{15}) \\
&= (HV_{Low}, CF_{Low}, M_{Low}, V_{Low}, HV_{Medium}, CF_{Medium}, \\
&\quad M_{Medium}, V_{Medium}, HV_{High}, CF_{High}, M_{High}, V_{High}, \\
&\quad Risk_{Low},\ Risk_{Medium},\ Risk_{High}) \\
&= (0,\ 0.95,\ 0,\ 0,\ 0.82,\ 0.04,\ 0.51,\ 0,\ 0.17,\ 0,\ 0.48, \\
&\quad 0.93,\ 0,\ 0,\ 0)
\end{aligned}$$

for RA-FCM and

$$\begin{aligned}
A_{IRA-FCM} &= (C_1, C_2, C_3, C_4, C_5, C_6, C_7, C_8, C_9, C_{10}, C_{11}, C_{12}, C_{13}, \\
&\quad C_{14}, C_{15}) \\
&= (HV_{Low}, CF_{Low}, M_{Low}, V_{Low}, HV_{Medium}, CF_{Medium}, \\
&\quad M_{Medium}, V_{Medium}, HV_{High}, CF_{High}, M_{High}, V_{High}, \\
&\quad Risk_{Low},\ Risk_{Medium},\ Risk_{High}) \\
&= (\langle 0, 0.82\rangle, \langle 0.95, 0.04\rangle, \langle 0, 0.51\rangle, \langle 0, 0.93\rangle, \langle 0.82, 0.17\rangle \\
&\quad, \langle 0.04, 0.95\rangle, \langle 0.51, 0.48\rangle, \langle 0, 0, 93\rangle, \langle 0.17, 0.82\rangle, \\
&\quad \langle 0, 0.95\rangle, \langle 0.48, 0.51\rangle, \langle 0.93, 0\rangle, \langle 0, 1\rangle, \langle 0, 1\rangle, \langle 0, 1\rangle)
\end{aligned}$$

for IRA-FCM.

Then, both the RA-FCM and the IRA-FCM iteratively calculate their concept values, until they reach a steady state, after $\boldsymbol{t} = \mathbf{10}$ iterations. The convergence of the output concepts of the RA-FCM and the IRA-FCM models, in terms of their membership and hesitancy values, is illustrated in Fig. 11, Fig 12 and Fig. 13 respectively. The results of the risk assessment are presented in Fig 14. In Figs. 11-14 output concepts C_{13}, C_{14}, C_{15} are associated with $Risk_{Low},\ Risk_{Medium},\ Risk_{High}$, respectively.

In Fig. 14, the blue bars represent membership of RA-FCM, orange bars represent membership of IRA-FCM, grey bars represent non-membership of IRA-FCM and yellow bars represent the respective hesitancy values of IRA-FCM. It can

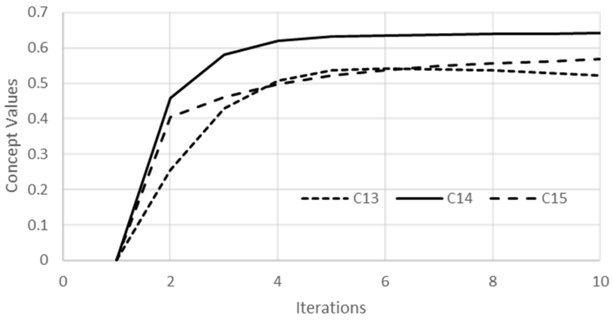

FIGURE 11. Membership convergence of RA-FCM during reasoning.

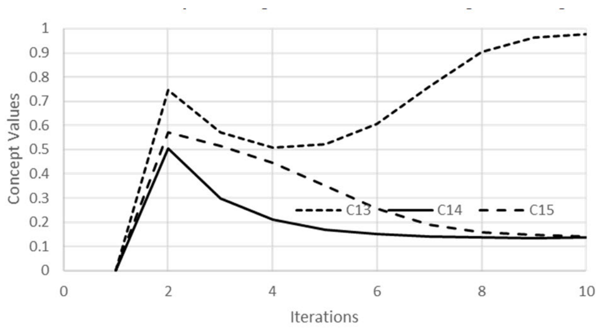

FIGURE 12. Membership convergence of IRA-FCM during reasoning.

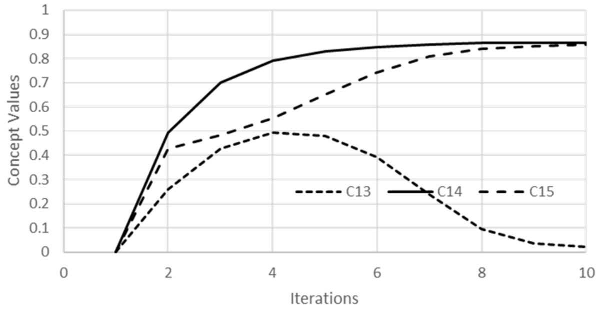

FIGURE 13. Hesitancy convergence of IRA-FCM during reasoning.

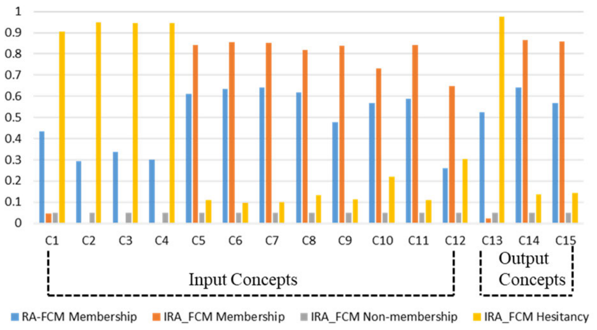

FIGURE 14. Membership, nonmembership, hesitancy values for concepts at $t = 10$ for RA-FCM and IRA-FCM.

be observed that in all cases, the non-membership values reach zero at the steady state. This outcome is a result of the reasoning process governed by Eq. 7 [37], demonstrating that initial non-membership values do not significantly influence the final decision. Furthermore, the hesitancy values decrease for IRA-FCM nodes that contain information related to similar risk levels.

As illustrated in Fig. 11-Fig. 14, a comparative analysis between RA-FCM and IRA-FCM reveals notable differences in the accuracy and interpretability of risk level classification within the monitoring environment. Based on Fig. 11 the risk of the monitoring environment obtained after convergence is classified as medium (C14) using RA-FCM, however, the method also yields relatively high membership degrees for low (C13) and high risk levels (C15), indicating a significant degree of uncertainty and overlap among these categories. On the contrary, Fig. 12 illustrates the enhanced discriminative capability of IRA-FCM, which yields a more accurate risk prediction, as it accounts for the overlap between medium and high risk—an overlap illustrated in Fig. 10. Notably, in Fig. 13 the hesitancy values corresponding to medium and high risks are similar, reinforcing this overlap and supporting IRA-FCM's enhanced predictive capability. Also, Fig. 14 shows that using IRA-FCM, the membership values of concepts C13-C15 that represent risk levels, are closer to zero than the similar of RA-FCM. This demonstrates that IRA-FCM can more effectively learn and represent the inter-concept relationships, leading to more precise risk assessments.

V. CONCLUSION

In this paper, a novel framework named IRA-FCM was introduced. The proposed framework constructs an intuitionistic FCM for interpretable risk assessment and to the best of our knowledge it is the first data-driven approach for disease transmission risk assessment in ventilated indoor spaces. The presented case study was focused on SARS-CoV-2 transmission in cruise ships; however, the proposed framework is directly applicable in similar use cases, that include transmission of other airborne diseases in ventilated indoor spaces with resident populations, such as apartment buildings, hotels and hospitals. The outcomes of the experiments demonstrated the effectiveness of IRA-FCM to construct data driven intuitionistic FCM classifiers for different data features to determine the risk level of a monitoring environment. In addition, unlike relevant risk assessment methods it is inherently interpretable.

The main advantages of the proposed IRA-FCM can be summarized as:

- It can be easily adapted to different contexts of risk assessment based on the collected data.
- It provided interpretable inference using the reasoning process and provides information about the hesitation of the decisions.
- It is easily integrable to applications for the integration of multi-source information, which has been collected from various sensors and the ship's information system, and it is in alignment with smart ship design.

Beyond the theoretical formulation and experimental evaluation, the proposed IRA-FCM framework can be readily translated into practical applications. It can be integrated into real-time monitoring platforms on ships or buildings, using data from existing sensors (*e.g.*, CO_2, ventilation rates, occupancy) to provide continuous, interpretable risk estimates that support operational decisions. Moreover, the framework could be used by operators to test "what-if" scenarios, such as adjusting ventilation or modifying occupancy, to evaluate the impact of different mitigation strategies.

A limitation of the proposed framework is that its real-world application depends on actual training data that are challenging to collect during real outbreaks. The dependence on simulated data remains the primary limitation of the current study, as it may not fully capture the complexity and variability of real-world conditions. However, considering the approximate reality provided by the simulated data, their use for training IRA-FCM either solely or in conjunction with actual data acquired during real outbreaks, could be sufficient for risk assessment in real-world conditions. Moreover, the results from the LOEO experiments revealed the challenge of achieving consistent cross-environment generalization, indicating that model performance may vary when applied to previously unseen environments. Nevertheless, this needs to be further investigated in future long-term studies, involving expanded datasets and real-world deployments to enhance both data representativeness and model generalizability.

Future work will address this challenge by investigating model transferability and stability across multiple environments. Additionally, future research will include exploring other applications of RA-FCM and IRA-FCM in diverse risk assessment contexts, such as health and safety, climate risk, credit and market risks, and cybersecurity. Further improvements may focus on enhancing IRA-FCM reasoning processes and alternative approaches for modeling non-membership or hesitancy.

REFERENCES

[1] P. Kumar, S. Hama, H. Y. W. Cheung, C. Hadjichristodoulou, V. A. Mouchtouri, L. Anagnostopoulos, L. Kourentis, Z. Wang, E. R. Galea, J. Ewer, A. Grandison, F. Jia, and N. Siilin, "Airborne pathogen monitoring and dispersion modelling on passenger ships: A review," *Sci. Total Environ.*, vol. 980, Jun. 2025, Art. no. 179571.

[2] G. Triantafyllou, P. G. Kalozoumis, E. Cholopoulou, and D. K. Iakovidis, "Disease spread control in cruise ships: Monitoring, simulation, and decision making," in *The Blue Book: Smart Sustainable Coastal Cities and Blue Growth Strategies for Marine and Maritime Environments*. Cham, Switzerland: Springer, 2024, pp. 93–141.

[3] P. Cheng, K. Luo, S. Xiao, H. Yang, J. Hang, C. Ou, B. J. Cowling, H.-L. Yen, D. S. Hui, S. Hu, and Y. Li, "Predominant airborne transmission and insignificant fomite transmission of SARS-CoV-2 in a two-bus COVID-19 outbreak originating from the same pre-symptomatic index case," *J. Hazardous Mater.*, vol. 425, Mar. 2022, Art. no. 128051.

[4] T. Dbouk and D. Drikakis, "On coughing and airborne droplet transmission to humans," *Phys. Fluids*, vol. 32, no. 5, May 2020, Art. no. 053310.

[5] M. El Hassan, H. Assoum, N. Bukharin, H. Al Otaibi, M. Mofijur, and A. Sakout, "A review on the transmission of COVID-19 based on cough/sneeze/breath flows," *Eur. Phys. J. Plus*, vol. 137, no. 1, pp. 1–16, Dec. 2021.

[6] V. Mihai and L. Rusu, "An overview of the ship ventilation systems and measures to avoid the spread of diseases," *Inventions*, vol. 6, no. 3, p. 55, Jul. 2021.

[7] P. Azimi, Z. Keshavarz, J. G. Cedeno Laurent, B. Stephens, and J. G. Allen, "Mechanistic transmission modeling of COVID-19 on the diamond princess cruise ship demonstrates the importance of aerosol transmission," *Proc. Nat. Acad. Sci. USA*, vol. 118, no. 8, Feb. 2021, Art. no. 2015482118.

[8] B. Batista, D. Dickenson, K. Gurski, M. Kebe, and N. Rankin, "Minimizing disease spread on a quarantined cruise ship: A model of COVID-19 with asymptomatic infections," *Math. Biosci.*, vol. 329, Nov. 2020, Art. no. 108442.

[9] K. Mizumoto and G. Chowell, "Transmission potential of the novel coronavirus (COVID-19) onboard the diamond Princess Cruises ship, 2020," *Infectious Disease Model.*, vol. 5, pp. 264–270, Jan. 2020.

[10] K. Mizumoto, K. Kagaya, A. Zarebski, and G. Chowell, "Estimating the asymptomatic proportion of coronavirus disease 2019 (COVID-19) cases on board the diamond princess cruise ship, Yokohama, Japan, 2020," *Eurosurveillance*, vol. 25, no. 10, Mar. 2020, Art. no. 2000180.

[11] M. Delikhoon, M. I. Guzman, R. Nabizadeh, and A. Norouzian Baghani, "Modes of transmission of severe acute respiratory syndrome-coronavirus-2 (SARS-CoV-2) and factors influencing on the airborne transmission: A review," *Int. J. Environ. Res. Public Health*, vol. 18, no. 2, p. 395, Jan. 2021.

[12] S. Rahn, M. Gödel, G. Köster, and G. Hofinger, "Modelling airborne transmission of SARS-CoV-2 at a local scale," *PLoS ONE*, vol. 17, no. 8, Aug. 2022, Art. no. e0273820.

[13] V. Vuorinen et al., "Modelling aerosol transport and virus exposure with numerical simulations in relation to SARS-CoV-2 transmission by inhalation indoors," *Saf. Sci.*, vol. 130, Oct. 2020, Art. no. 104866.

[14] L. Braidotti, S. Bertagna, M. Dodero, M. Piu, A. Marino, and V. Bucci, "Identification of measures to contain the outbreaks on passenger ships using pedestrian simulations," *Proc. Comput. Sci.*, vol. 200, pp. 1565–1574, Jan. 2022.

[15] N. P. Ventikos, P. Sotiralis, and M. Annetis, "Health risk assessment in maritime operations and ship design: A framework for addressing health-related risks in the context of maritime safety assessment," in *Proc. 7th Int. Conf. Transp. Inf. Saf. (ICTIS)*, Aug. 2023, pp. 2416–2424.

[16] Z. Wang, M. Yao, C. Meng, and C. Claramunt, "Risk assessment of the overseas imported COVID-19 of ocean-going ships based on AIS and infection data," *ISPRS Int. J. Geo-Inf.*, vol. 9, no. 6, p. 351, May 2020.

[17] *Tool for Influenza Pandemic Risk Assessment (TIPRA)*, WHO Organization, Geneva, Switzerland, 2016.

[18] R. K. Brewster, A. Sundermann, and C. Boles, "Lessons learned for COVID-19 in the cruise ship industry," *Toxicology Ind. Health*, vol. 36, no. 9, pp. 728–735, Sep. 2020.

[19] A.-C. Kordsmeyer, N. Mojtahedzadeh, J. Heidrich, K. Militzer, T. von Münster, L. Belz, H.-J. Jensen, S. Bakir, E. Henning, J. Heuser, A. Klein, N. Sproessel, A. Ekkernkamp, L. Ehlers, J. de Boer, S. Kleine-Kampmann, M. Dirksen-Fischer, A. Plenge-Bönig, V. Harth, and M. Oldenburg, "Systematic review on outbreaks of SARS-CoV-2 on cruise, navy and cargo ships," *Int. J. Environ. Res. Public Health*, vol. 18, no. 10, p. 5195, May 2021.

[20] Z. Xia, H. Guan, Z. Qi, and P. Xu, "Multi-zone infection risk assessment model of airborne virus transmission on a cruise ship using CONTAM," *Buildings*, vol. 13, no. 9, p. 2350, Sep. 2023.

[21] A. Elhanashi, S. Saponara, P. Dini, Q. Zheng, D. Morita, and B. Raytchev, "An integrated and real-time social distancing, mask detection, and facial temperature video measurement system for pandemic monitoring," *J. Real-Time Image Process.*, vol. 20, no. 5, p. 95, Oct. 2023.

[22] A. C. Makino Antunes, A. Aldred, G. P. Tirado Moreno, J. A. de Souza Ribeiro, P. E. Brandão, G. T. Barone, J. D. A. Conselheiro, A. C. Goulart, I. C. Desuó, and G. Gomes, "Potential of using facial thermal imaging in patient triage of flu-like syndrome during the COVID-19 pandemic crisis," *PLoS ONE*, vol. 18, no. 1, Jan. 2023, Art. no. e0279930.

[23] S. Wrotek, E. K. LeGrand, A. Dzialuk, and J. Alcock, "Let fever do its job: The meaning of fever in the pandemic era," *Evol., Med., Public Health*, vol. 9, no. 1, pp. 26–35, 2021.

[24] E. Altshuler, B. Tannir, G. Jolicoeur, M. Rudd, C. Saleem, K. Cherabuddi, D. H. Doré, P. Nagarsheth, J. Brew, P. M. Small, J. Glenn Morris, and S. Grandjean Lapierre, "Digital cough monitoring—A potential predictive acoustic biomarker of clinical outcomes in hospitalized COVID-19 patients," *J. Biomed. Informat.*, vol. 138, Feb. 2023, Art. no. 104283.

[25] G. Celik, "CovidCoughNet: A new method based on convolutional neural networks and deep feature extraction using pitch-shifting data augmentation for COVID-19 detection from cough, breath, and voice signals," *Comput. Biol. Med.*, vol. 163, Sep. 2023, Art. no. 107153.

[26] A. Pal and M. Sankarasubbu, "Pay attention to the cough: Early diagnosis of COVID-19 using interpretable symptoms embeddings with cough sound signal processing," in *Proc. 36th Annu. ACM Symp. Appl. Comput.*, Mar. 2021, pp. 620–628.

[27] B. Lebental, "Real-time, systematic disease detection on cruise ships: Feasibility assessment for outbreak prevention," in *The Blue Book: Smart Sustainable Coastal Cities and Blue Growth Strategies for Marine and Maritime Environments*. Cham, Switzerland: Springer, 2024, pp. 143–160.

[28] B. Kosko, "Fuzzy cognitive maps," *Int. J. Man-Mach. Stud.*, vol. 24, no. 1, pp. 65–75, 1986.

[29] A. Amirkhani, M. Kolahdoozi, C. Wang, and L. A. Kurgan, "Prediction of DNA-binding residues in local segments of protein sequences with fuzzy cognitive maps," *IEEE/ACM Trans. Comput. Biol. Bioinf.*, vol. 17, no. 4, pp. 1372–1382, Jul. 2020.

[30] P. P. Groumpos and I. D. Apostolopoulos, "Modeling the spread of dangerous pandemics with the utilization of a hybrid-statistical–advanced-fuzzy-cognitive-map algorithm: The example of COVID-19," *Res. Biomed. Eng.*, vol. 37, no. 4, pp. 749–764, Dec. 2021.

[31] C. Jiang, Z. Liu, Y. Wang, G. Yao, J. He, S. Li, R. Rong, Z. Liang, and J. Liu, "Severity and risk to inhalation of pathogen-laden aerosol in large public spaces: Insights from fangcang shelter hospitals under multi-location release," *J. Hazardous Mater.*, vol. 483, Feb. 2025, Art. no. 136695.

[32] Q. Jiang, X. Zhou, R. Wang, W. Ding, Y. Chu, S. Tang, X. Jia, and X. Xu, "Intelligent monitoring for infectious diseases with fuzzy systems and edge computing: A survey," *Appl. Soft Comput.*, vol. 123, Jul. 2022, Art. no. 108835.

[33] M. Kolahdoozi, A. Amirkhani, M. H. Shojaeefard, and A. Abraham, "A novel quantum inspired algorithm for sparse fuzzy cognitive maps learning," *Appl. Intell.*, vol. 49, no. 10, pp. 3652–3667, Oct. 2019.

[34] P. P. Groumpos, "Why modelling the COVID-19 pandemic using fuzzy cognitive maps (FCM)?" *IFAC-PapersOnLine*, vol. 54, no. 13, pp. 305–310, 2021.

[35] R. Schuerkamp and P. J. Giabbanelli, "Extensions of fuzzy cognitive maps: A systematic review," *ACM Comput. Surv.*, vol. 56, no. 2, pp. 1–36, Feb. 2024.

[36] D. K. Iakovidis and E. Papageorgiou, "Intuitionistic fuzzy cognitive maps for medical decision making," *IEEE Trans. Inf. Technol. Biomed.*, vol. 15, no. 1, pp. 100–107, Jan. 2011.

[37] E. I. Papageorgiou and D. K. Iakovidis, "Intuitionistic fuzzy cognitive maps," *IEEE Trans. Fuzzy Syst.*, vol. 21, no. 2, pp. 342–354, Apr. 2013.

[38] P. Hajek, W. Froelich, and O. Prochazka, "Intuitionistic fuzzy grey cognitive maps for forecasting interval-valued time series," *Neurocomputing*, vol. 400, pp. 173–185, Aug. 2020.

[39] A. Amirkhani, E. I. Papageorgiou, M. R. Mosavi, and K. Mohammadi, "A novel medical decision support system based on fuzzy cognitive maps enhanced by intuitive and learning capabilities for modeling uncertainty," *Appl. Math. Comput.*, vol. 337, pp. 562–582, Nov. 2018.

[40] S. Bueno and J. L. Salmeron, "Benchmarking main activation functions in fuzzy cognitive maps," *Expert Syst. Appl.*, vol. 36, no. 3, pp. 5221–5229, Apr. 2009.

[41] K. T. Atanassov and K. T. Atanassov, *Intuitionistic Fuzzy Sets*. Cham, Switzerland: Springer, 1999.

[42] P. Angelov, "Crispification: Defuzzification of intuitionistic fuzzy sets," *Busefal*, vol. 64, pp. 51–55, Mar. 1995.

[43] G. Sovatzidi, G. Triantafyllou, G. Dimas, P. G. Kalozoumis, D. Drikakis, I. W. Kokkinakis, I. Markakis, C. Golna, and D. K. Iakovidis, "Risk assessment of COVID-19 transmission on cruise ships using fuzzy rules," in *Proc. IFIP Int. Conf. Artif. Intell. Appl. Innov.*, 2024, pp. 336–348.

[44] G. Triantafyllou, G. Sovatzidi, G. Dimas, P. G. Kalozoumis, D. Drikakis, I. W. Kokkinakis, I. A. Markakis, C. Golna, and D. K. Iakovidis, "Sensor-based fuzzy inference of COVID-19 transmission risk in cruise ships," in *Proceedings Medical Informatics Europe (MIE), Public Health and Informatics*. Amsterdam, The Netherlands: IOS Press, 2024.

[45] T. Dbouk and D. Drikakis, "On respiratory droplets and face masks," *Phys. Fluids*, vol. 32, no. 6, Jun. 2020, Art. no. 063303, doi: 10.1063/5.0015044.

[46] J. Drake and G. Hamerly, "Accelerated K-means with adaptive distance bounds," in *Proc. 5th NIPS Workshop Optim. Mach. Learn.*, vol. 8, 2012, pp. 1–4.

MICHAEL D. VASILAKAKIS received the Ph.D. degree from the Department of Computer Science and Biomedical Informatics, University of Thessaly, Greece, in 2020. Currently, he is a Postdoctoral Researcher with the Biomedical Imaging Laboratory, University of Thessaly. His research interests include signal and image processing, decision support systems, fuzzy logic, interpretable and explainable machine learning, and applications. In this context, he has co-authored over 20 papers in international journals, conferences, and books.

GEORGIOS TRIANTAFYLLOU received the B.Sc. degree in computer science and biomedical informatics from the University of Thessaly, Greece, in 2018, and the M.Sc. degree in complex adaptive systems from the Chalmers University of Technology, Sweden, in 2021. He is currently pursuing the Ph.D. degree in computational modelling of complex systems using machine learning with the University of Thessaly.

From 2018 to 2019, he was a Software Engineer, developing web applications. His research interests include the development of machine learning and deep learning models for computational modeling and simulation of complex systems.

DIMITRIS K. IAKOVIDIS (Senior Member, IEEE) received the Ph.D. degree from the Department of Informatics and Telecommunications, University of Athens, Greece, in 2004. In 2015, he was an Associate Professor with the Department of Computer Science and Biomedical Informatics, University of Thessaly, Greece. Currently, he is a Professor and the Director of the Biomedical Imaging Laboratory. His research interests include signal and image processing, decision support systems, intelligent systems, and applications. In this context, he has co-authored over 200 papers in international journals, conferences, and books. He served as an Associate Editor for IEEE TRANSACTIONS ON FUZZY SYSTEMS and *IET Signal Processing*. He is an Editorial Board Member of *Measurement Science and Technology* journal.

• • •